Modeling of Rayleigh-Taylor mixing using single-fluid models

Ioannis W. Kokkinakis,[1,*] Dimitris Drikakis,[2,†] and David L. Youngs[1,‡]
[1]*Department of Mechanical and Aerospace Engineering, University of Strathclyde, Glasgow G1 1XJ, United Kingdom*
[2]*University of Nicosia, Nicosia CY-2417, Cyprus*

(Received 24 February 2018; published 9 January 2019)

Turbulence mixing models of different degree of complexity are investigated for Rayleigh-Taylor mixing flows with reference to high-resolution implicit large eddy simulations. The models considered, in order of increasing complexity, comprise the (i) two-equation *K-L*, (ii) three-equation *K-L-a*, (iii) four-equation *K-L-a-b*, and (iv) Besnard-Harlow-Rauenzahn (BHR-2). The above models are implemented in the same numerical framework to minimize the computational uncertainty. The impact of the various approximations represented by the different models is investigated for canonical one-dimensional (1D) Rayleigh-Taylor mixing and for the more complex (2D on average) case of the tilted-rig experiment, aiming to understand the balance between accuracy and complexity. The results provide guidance on the relative merits of various turbulence models over a variety of conditions.

DOI: 10.1103/PhysRevE.99.013104

I. INTRODUCTION

The Rayleigh-Taylor (RT) instability occurs in a wide range of variable-density flows, both natural and human-made, including inertial confinement fusion (ICF) [1,2], cavitation [3], combustion [4], astrophysics [5–8], and geophysical flows [9].

Although significant progress has been made in understanding RT mixing by using different simulation approaches, including direct numerical simulation (DNS) and large eddy simulation (LES), these approaches remain computationally expensive for complex applications such as ICF at high Reynolds numbers [10–22]. For complex applications, turbulence models based on transport equations, which predict the "average" behavior of the turbulent mixing zone, are employed. Turbulence models allow for larger time steps and coarser computational grids than DNS and LES. Furthermore, for cases where the average behavior has homogeneous directions, the computational cost can be further reduced by performing calculations in preferential directions. Due to the ensemble averaging of the second- and higher-order correlations of turbulent fluctuations, additional terms arise that require modeling. The modeling assumptions and closure coefficients are validated and calibrated through comparisons with experiments but increasingly through comparisons with high-resolution simulations because quantitative experimental data are limited.

Turbulence mixing models can be classified into three categories. The simplest models are called buoyancy drag models [23–26] and use ordinary differential equations to evolve the width of the mixing layer. The bubble, or spike, amplitudes are described by balancing the inertia, buoyancy, and drag forces. These models cannot model multiple mixing interfaces; cannot be easily extended to two and three dimensions; and, as a rule, do not address demixing, also known as countergradient transport, i.e., reduction of total fluid masses within the mixing zone. To address the above problems, two-fluid (or multi-fluid) models have been proposed [27–30]. They use a separate set of equations for each fluid in addition to the main flow equations and provide an accurate modeling framework for demixing by correctly capturing the relative motion of the different fluid fragments. An intermediate class of models are the single-fluid models [31–34]. They consist of evolutionary equations for the turbulence kinetic energy and its dissipation rate or equivalent turbulence length scale.

A more advanced version of the single-fluid models is the Besnard-Harlow-Rauenzahn (BHR) model [35]. The BHR model is based on the evolution equations arising from second-order correlations and gradient-diffusion approximations. Using a mass-weighted averaged decomposition, the original BHR model includes full transport equations for the Reynolds stresses, turbulent mass-flux velocity, density fluctuations, and the turbulence kinetic energy dissipation rate. Several efforts were made to simplify the resulting equations. A three-equation variant was proposed for RT, Kelvin-Helmholtz (KH), and Richtmyer-Meshkov (RM) flows [36]. A second-moment closure implementation was also presented by Schwarzkopf *et al.* [37]. In the present study, the four-equation variant, known as the BHR-2 model [38], was employed. The BHR-2 model is also investigated here in conjunction with the modified species turbulent diffusion term [39], which can improve accuracy in demixing.

Despite the aforementioned efforts, there is still an uncertainty over the optimum choice of turbulence models, a lack of systematic comparison between the different models, as well as room for significantly improving the models accuracy across flow regimes. In this study, specific modifications to the original models that result in improved accuracy are proposed. A systematic comparison of the accuracy of the different

*ioannis.kokkinakis@strath.ac.uk
†drikakis.d@unic.ac.cy
‡david.youngs@strath.ac.uk

models is presented for canonical planar RT flows [16,18] and the tilted-rig experiment [27,40].

II. TURBULENCE MIXING MODELS

The first step for the development of turbulence models is to perform Reynolds averaging of the governing equations and Favre averaging of the resultant terms. As in previous studies [27–29,31,32,36,38], high-Reynolds-number applications are considered where turbulent viscosity, conductivity, and diffusivity are large compared to molecular values.

The resulting modeled governing equations of the mixture are given by:

$$\frac{\partial \bar{\rho}}{\partial t} + \frac{\partial \bar{\rho}\tilde{u}_j}{\partial x_j} = 0, \tag{1}$$

$$\frac{\partial \bar{\rho}\tilde{u}_i}{\partial t} + \frac{\partial}{\partial x_j}(\bar{\rho}\tilde{u}_i\tilde{u}_j + \bar{p}\delta_{ij}) = \frac{\partial \tau_{ij}}{\partial x_j} + \bar{\rho}g_j, \tag{2}$$

$$\frac{\partial \bar{\rho}\tilde{E}}{\partial t} + \frac{\partial(\bar{\rho}\tilde{E} + \bar{p})\tilde{u}_j}{\partial x_j} = \frac{\partial \tau_{ij}\tilde{u}_i}{\partial x_j} + \bar{\rho}\tilde{u}_j g_j - \frac{\partial q_j}{\partial x_j} + \frac{\partial}{\partial x_j}\left(\frac{\mu_t}{N_K}\frac{\partial K}{\partial x_j}\right), \tag{3}$$

$$\frac{\partial \bar{\rho}\tilde{F}}{\partial t} + \frac{\partial \bar{\rho}\tilde{F}\tilde{u}_j}{\partial x_j} = -\frac{\partial J_j}{\partial x_j}, \tag{4}$$

where variables labeled by "bar" and "tilde" denote Reynolds and Favre averages, respectively; ρ is the density; u_i are the velocity components; F is the mass fraction; and E is the total energy. The repeated index j implies summation over the dimensions $(i, j) = 1, 2, 3$; g_j is an external acceleration in the direction of dimension j; and μ_t is the eddy viscosity.

The perfect gas assumption is employed, $\bar{p} = \bar{\rho}R_*\tilde{T}$, where R_* is the mixture specific gas constant and $\tilde{T}$ is the Favre-averaged static temperature corresponding to the static pressure (conditions) of the mixture.

The Favre-averaged total energy is obtained from the sum of the Favre-averaged internal energy, kinetic energy, turbulence kinetic energy, and potential energy:

$$\tilde{E} = \tilde{e} + \frac{\tilde{u}_k\tilde{u}_k}{2} + K + g_j x_j, \tag{5}$$

where $\tilde{e} = \bar{p}/(\gamma - 1)\bar{\rho}$ is the Favre-averaged internal energy per unit mass.

Using the isobaric assumption for the thermodynamic closure of the mixture [41], the heat capacity ratio of the mixture γ is calculated by:

$$\gamma = 1 + \frac{1}{\sum_{n=1}^{N}\frac{f_n}{\gamma_n - 1}}, \tag{6}$$

where N is the total number of the species and γ_n is the heat capacity ratio of a component n. The volume fraction of species n, f_n, is calculated by:

$$f_n = \frac{F_n/M_n}{\sum_{m=1}^{N} F_m/M_m}, \tag{7}$$

where F_n and M_n are its mass fraction and molar mass, respectively, and $\sum_{m=1}^{N} f_m = 1$.

The turbulent diffusion terms are adjusted using dimensionless scaling factors such that N_h and N_F correspond to the turbulent Prandtl ($\mathrm{Pr}_t = c_p\mu_t/\kappa_t$) and Schmidt ($\mathrm{Sc}_t = \mu_t/(\rho D_t)$) numbers, respectively. Note that the turbulent transport (diffusion) of the turbulence kinetic energy is also accounted for in Eq. (3).

There are also extra terms arising from the Favre averaging that need to be modeled: (i) the Reynolds stress tensor $\tau_{ij} \equiv -\overline{\rho u_i'' u_j''}$, (ii) the turbulent viscosity μ_t, and (iii) the density weighted turbulence kinetic energy $K \equiv \tilde{k} = \widetilde{u_k'' u_k''}/2 = \overline{\rho u_k'' u_k''}/2\bar{\rho} = -\tau_{ii}/2\bar{\rho}$.

The transport equation for the Favre-averaged turbulence kinetic energy is given by:

$$\frac{\partial \bar{\rho}K}{\partial t} + \frac{\partial \bar{\rho}K\tilde{u}_j}{\partial x_j} = S_K + \tau_{ij}\frac{\partial \tilde{u}_i}{\partial x_j} + \frac{\partial}{\partial x_j}\left(\frac{\mu_t}{N_K}\frac{\partial K}{\partial x_j}\right) - \bar{\rho}\varepsilon, \tag{8}$$

where N_K is the scaling factor for the turbulence kinetic energy diffusion and ε is the dissipation:

$$\varepsilon = C_D\, u_t^3/L. \tag{9}$$

C_D is the drag coefficient and $u_t = \sqrt{2K}$ is the turbulent velocity. Equation (8) varies across models depending on the formulation of the turbulence kinetic energy production source term, S_K.

For the turbulent transport terms in the mass fraction and total energy equations, the diffusivities of all species are assumed to be the same [42]. Assuming Fickian diffusion, the turbulent mass flux of species n is given by:

$$J_{n,j} = -\frac{\mu_t}{N_F}\frac{\partial \tilde{F}_n}{\partial x_j} \tag{10}$$

and for the case of two fluids:

$$J_j \equiv J_{1,j} = -J_{2,j} = -\frac{\mu_t}{N_F}\frac{\partial \tilde{F}}{\partial x_j}. \tag{11}$$

The internal energy flux, q_j [43,44], is obtained from adding the interdiffusional enthalpy flux:

$$q_j^d = \sum_{n=1}^{N} \tilde{h}_n J_{n,j}, \tag{12}$$

where $\tilde{h}_n$ is the specific enthalpy of species n and the turbulent heat conduction flux, q_j^c:

$$q_j^c = -\bar{\rho}D_T c_p \frac{\partial \tilde{T}}{\partial x_j}, \tag{13}$$

where c_p is the mixture's specific heat capacity at constant pressure:

$$c_p = \sum_{n=1}^{N} c_{pn}F_n.$$

If the heat conductivity, D_T, is set equal to the species turbulent diffusivity, $\mu_t/(\bar{\rho}N_F)$, and the fluid species have constant specific heats, then the internal energy flux is simplified (see Kokkinakis *et al.* [42]) as

$$q_j = q_j^d + q_j^c = -\frac{\mu_t}{N_F}\frac{\partial \tilde{h}}{\partial x_j}, \tag{14}$$

where $\tilde{h} = \gamma\tilde{e}$ is the Favre-averaged specific enthalpy of the mixture. Equations (11) and (14) are used in the averaged governing equations of the species mass fraction (4) and total energy (3), respectively.

The set of equations is completed by an equation for the turbulence length scale, $L \equiv C_D K^{3/2}/\varepsilon$ [37]:

$$\frac{\partial \bar{\rho} L}{\partial t} = -\frac{\partial \bar{\rho} L \tilde{u}_j}{\partial x_j} + C_L \rho u_t + C_C \bar{\rho} L \frac{\partial \tilde{u}_j}{\partial x_j} + \frac{\partial}{\partial x_j}\left(\frac{\mu_t}{N_L}\frac{\partial L}{\partial x_j}\right), \tag{15}$$

where on the right-hand side the second, third, and last terms are used to model production, compressibility effects, and turbulent diffusion, respectively, where $C_L = 1$ and $C_C = 1/3$. The rest of the model constants are given in the Appendix.

The eddy viscosity is calculated by:

$$\mu_t = C_\mu \bar{\rho} u_t L, \tag{16}$$

where C_μ is a constant.

All turbulence mixing models are calibrated using the full Reynolds stress tensor based on the Boussinesq eddy-viscosity assumption:

$$\tau_{ij} = \mu_t\left(\frac{\partial \tilde{u}_j}{\partial x_i} + \frac{\partial \tilde{u}_i}{\partial x_j} - \frac{1}{3}\frac{\partial \tilde{u}_k}{\partial x_k}\delta_{ij}\right) - \frac{2}{3}\bar{\rho} K \delta_{ij}. \tag{17}$$

A. $K - L$ model

The K-L model was proposed by Dimonte and Tipton [32] for describing the turbulent self-similar regime of RT and RM induced mixing. The starting point for deriving the model equations are the buoyancy-drag models for the self-similar growth of RT and RM instabilities [23,25]. Here an improved version of the model proposed by Kokkinakis *et al.* [42] is used based on the following modifications: (i) a transport equation for the total energy, Eq. (3), instead of the internal energy; (ii) the turbulent diffusion of specific enthalpy instead of internal energy in Eq. (3); (iii) the implementation of the source term (S_K) in Eq. (8) based on the mean flow and turbulence timescales; and (iv) the calculation of the local Atwood number based on higher-order numerical approximations.

B. $K - L - a$ model

The three-equation model of Morgan and Wickett [45] was developed as an extension to the two-equation K-L model of Dimonte and Tipton [32] by including a third equation for the turbulent mass-flux velocity, $a_i \equiv \overline{\rho' u_i'}/\bar{\rho} = -\overline{u_i''}$.

The production source term of the turbulence kinetic energy is given by:

$$S_K = C_B a_j \frac{\partial \bar{p}}{\partial x_j}, \tag{18}$$

and the governing equation for the mass-flux velocity is written as

$$\frac{\partial \bar{\rho} a_i}{\partial t} = -\frac{\partial \bar{\rho}\tilde{u}_j a_i}{\partial x_j} + b\frac{\partial \bar{p}}{\partial x_i} + \frac{\tau_{ij}}{\bar{\rho}}\frac{\partial \bar{\rho}}{\partial x_j} + \frac{\partial}{\partial x_j}\left(\frac{\mu_t}{N_a}\frac{\partial a_i}{\partial x_j}\right) - C_{Da}\bar{\rho} a_i \frac{u_t}{L}. \tag{19}$$

The density-specific volume covariance, $b \equiv -\overline{\rho'(1/\rho)'}$, is a (positive) measure of the molecular mixing state of the mixture. An algebraic expression generalized for an n-component mixture and includes an added-mass correction factor, c, is [45]

$$b = \bar{\rho}\frac{\sum_n \frac{f_n}{\rho_n + c\bar{\rho}}}{\sum_n \frac{f_n \rho_n}{\rho_n + c\bar{\rho}}} - 1, \tag{20}$$

where c is determined from the implicit large eddy simulations (iLES). For perfectly molecularly mixed fluids $b = 0$, whereas for two immiscible fluids, b attains a maximum value given by a simple two-fluid formulation [36]:

$$b = f_1 f_2 \frac{(\rho_1 - \rho_2)^2}{\rho_1 \rho_2}, \tag{21}$$

where f_1 and f_2 are the volume fractions associated with the fluids composing the binary mixture and can be obtained by setting $c = 0$ in Eq. (20). Positive values of c allow for some adjustment to the maximum value of b. Neither a miscible fluids formulation for the algebraic estimation of b nor the added-mass correction factor, c, is known.

Morgan *et al.* [46] have recently extended the K-L-a model to include a second length-scale equation, which relies on separating the turbulence transport ($L_t \equiv L$) and turbulence destruction (L_d) length scales. This is similar to the work carried out by Schwarzkopf *et al.* [47] for the BHR-3.1 model. The two-length-scale approach is necessary in order to simultaneously capture the growth parameter and turbulence intensity of a Kelvin-Helmholtz shear layer when model coefficients are constrained by similarity analysis.

C. $K - L - a - b$ model

We have extended here the K-L-a model by adding an evolution equation for the density-specific volume covariance (b). Examining Eq. (19) shows that b governs the primary production mechanism of the turbulent mass-flux and, therefore, needs to be modeled accurately to reflect the effects of the changes in the density fluctuations [38].

The governing equation for b employed here is similar to the BHR-2 model [38,48,49], but with the redistribution term omitted, as per Morgan and Wickett [45] with respect to a in Eq. (19):

$$\frac{\partial \bar{\rho} b}{\partial t} = -\frac{\partial \bar{\rho}\tilde{u}_j b}{\partial x_j} - 2(b+1)a_j\frac{\partial \bar{\rho}}{\partial x_j} + \bar{\rho}^2\frac{\partial}{\partial x_j}\left(\frac{\mu_t}{\bar{\rho}^2\sigma_b}\frac{\partial b}{\partial x_j}\right) - C_{Db}\frac{u_t}{L}b, \tag{22}$$

where the remaining terms on the right-hand side are the advection, production, turbulent diffusion, and destruction

terms, respectively. The *K-L-a-b* is essentially a reduced form of the BHR-2 model presented in the next section.

D. BHR-2 model

The basic formulation for the BHR model can be found in the paper by Besnard *et al.* [48] but several variants have also been proposed. The BHR-2 variant, considered in this study, uses an algebraic closure for the Reynolds stresses and the gradient diffusion approximation for the turbulent fluxes. An extensive review of the BHR-2 model can be found in Refs. [38,49,50]. The model introduces several additional terms in the governing equations of the turbulence length scale (L), turbulent mass-flux velocity (a_i), and density-specific volume covariance (b).

For the turbulence length scale, the model omits the compression term but adds two additional terms associated with net production:

$$\frac{\partial \bar{\rho} L}{\partial t} = \text{right-hand side [of (15)]} - C_C \bar{\rho} L \frac{\partial \tilde{u}_j}{\partial x_j} + \frac{L}{K}\left[C_{L4}\left(a_j \frac{\partial \bar{p}}{\partial x_j} \right) + C_{L1}\left(\tau_{ij} \frac{\partial \tilde{u}_i}{\partial x_j} \right) \right], \quad (23)$$

where $C_{L4} = (3/2 - C_4)$ and $C_{L1} = (3/2 - C_1)$.

For the turbulent mass-flux velocity, an additional production term and a redistribution term are included:

$$\frac{\partial \bar{\rho} a_i}{\partial t} = \text{right-hand side [of (19)]} - C_{Ba} \bar{\rho} a_j \frac{\partial (\tilde{u}_i - a_i)}{\partial x_j} + C_{Ra} \bar{\rho} \frac{\partial a_i a_j}{\partial x_j}. \quad (24)$$

Finally, a redistribution term is also included for the density-specific-volume covariance:

$$\frac{\partial \bar{\rho} b}{\partial t} = \text{right-hand side [of (22)]} + 2 C_{Rb} \bar{\rho} a_j \frac{\partial b}{\partial x_j}. \quad (25)$$

In this study, the model is implemented in conjunction with the total energy ($\tilde{E}$) instead of the specific internal energy ($\tilde{e}$). This is similar to the BHR-3 model [37,48] and its two-length-scale variant BHR-3.1 [47]. Using the same equation for $\tilde{E}$ for all turbulence models considered here allows for a more meaningful and direct comparison between the different turbulence models to be carried out.

The gradient diffusion approximation (GDA) is typically used to model the turbulent transport terms; for the species mass fraction it is defined as:

$$-\frac{\partial}{\partial x_j}(\overline{\rho u_j'' F''}) = \frac{\partial}{\partial x_j}\left(\frac{\mu_t}{N_F} \frac{\partial \tilde{F}}{\partial x_j} \right). \quad (26)$$

Bertsch and Gore [39] developed a modified species turbulent diffusion (MSTD) term and applied it in the framework of the second moment closure BHR-3.1 model. MSTD enables counter gradient transport and can model demixing in both BHR-3 and BHR-3.1 models. According to Ref. [39], the turbulent transport term on the right-hand side of Eq. (4) can be formulated in the incompressible limit as:

$$-\frac{\partial}{\partial x_j}(\overline{\rho u_j'' F''}) = \left(\frac{\rho_1 \rho_2}{\rho_2 - \rho_1} \right) \frac{\partial a_j}{\partial x_j}. \quad (27)$$

MSTD requires the turbulent mass-flux velocity (a_i) and partial densities, therefore, it can be implemented in any model that includes a transport equation for a_i. Results for the BHR-2 model using the MSTD, as well as the GDA (with and without the S_F limiter), are shown in relation to the tilted-rig case only because the results were identical for the one-dimensional (1D) problem.

E. Implementation details

The realizability conditions of Vreman *et al.* [51] are imposed on the Reynolds stresses:

$$\tau_{ii} \leqslant 0, \quad |\tau_{ij}| \leqslant (\tau_{ii}\tau_{jj})^{1/2}$$
$$\det(\tau_{ij}) \geqslant 0, \quad |\tau_{ij}| \leqslant 2\bar{\rho} K, \quad (28)$$

where the Reynolds stress tensor is $\tau_{ij} \equiv -\overline{\rho u_i'' u_j''}$.

Since all the models investigated employ the (Boussinesq) eddy-viscosity assumption for modeling τ_{ij}, and the GDA for modeling the turbulent transport terms, excessive turbulent diffusion can occur in locations of the flow that exhibit strong two-dimensional behavior. This can be interpreted as an overestimation of the turbulent diffusion in the direction normal to the local shear. Thus, in all of the two-dimensional simulations performed here, the turbulent viscosity is calculated by:

$$\mu_t = S_F (C_\mu \bar{\rho} u_t L), \quad (29)$$

where

$$S_F = 1 - \frac{|\tilde{u}_l|}{|\tilde{u}_m| + (1 - s_f)(|\tilde{u}_l| + u_t)},$$

and $\tilde{u}_m$ and $\tilde{u}_l$ are the local velocities parallel and normal to the direction of the flux, respectively; the subscript index corresponds to Eqs. (1)–(4) according to $m = j$ and $n \neq j$. Finally, s_f is given by

$$s_f = \min(1, |\tilde{u}_j + u_t|/\tilde{c}),$$

where $\tilde{c} = \sqrt{\gamma \bar{p}/\bar{\rho}}$ is the local speed of sound. Note that for computational stability, it is recommended to limit S_F above zero, i.e., $S_F = \max(0.01, S_F)$. The turbulent viscosity limiter S_F acts to reduce the turbulence diffusion via a reduction in the magnitude of the turbulent viscosity μ_t when velocity shearing is large. This can be partly justified by the smaller C_μ value required for modeling Kelvin-Helmholtz induced mixing, where typically a value of 0.09 is used [32].

Assuming a Cartesian grid, the local time-step size is calculated by:

$$\Delta t_l = \frac{\Delta x}{\tilde{c} + \|\tilde{\boldsymbol{u}}\| + u_D}, \quad (30)$$

where $\|\tilde{\boldsymbol{u}}\| = \sqrt{\tilde{u}_i^2}$ and i implies summation. The above formula takes into account the maximum turbulent diffusion velocity (u_D). This term needs to be included in the calculation of the global time step in order to maintain numerical stability; u_D is given by:

$$u_D = \frac{\mu_t}{\bar{\rho}} \times \max\left(\frac{|\partial \phi / \partial x_i|}{N_\phi \phi} \right), \quad (31)$$

where ϕ denotes $\tilde{h}$, K, or L. The global time step for updating the solution at each time iteration is the minimum local time-step value calculated in the domain, i.e., $\Delta t = \min(\Delta t_l)$.

The inclusion of u_D in the calculation of the time-step size is particularly important in the case of large values of turbulent viscosity and in the regions of steep gradients for quantities such as $\tilde{h}$, K, or L. For example, for simulations with CFL = 0.2 and without using u_D, the results become erroneous at late times of the mixing process, e.g., the total turbulent kinetic energy (TKE) begins to decrease. This behavior cannot be rectified by simply reducing the CFL number, as this would be case dependent. Including u_D in the definition of the time step reverts the total TKE to the correct physical behavior, even for larger CFL values, e.g., CFL = 0.3.

The models presented in the preceding sections have been numerically implemented using a finite volume Godunov-type [52] upwind, shock-capturing method in conjunction with

(i) the isobaric mixture assumption to estimate the heat capacity ratio of the mixture Eq. (6);

(ii) the fifth-order MUSCL scheme [53] in combination with a low Mach correction [54] for reconstructing the variables $[\bar{\rho}(1-\tilde{F}), \bar{\rho}\tilde{\boldsymbol{u}}, \bar{p}, \bar{\rho}\tilde{F}, \bar{\rho}K, \bar{\rho}L]$;

(iii) the HLLC Riemann solver [55] based on the pressure-based wave speed estimate method for the solution of the numerical intercell flux estimation;

(iv) a third-order total-variation-diminishing (TVD) Runge-Kutta scheme for time integration; see Refs. [56–59] and references therein.

The above numerical framework does not cause spurious numerical oscillations at the fluid interface, including the case of different heat capacity ratios ($\gamma_1 \neq \gamma_2$) [42].

III. 1D RAYLEIGH-TAYLOR MIXING

The turbulence models have been applied to the simulation of simple 1D RT mixing cases with a 3:1 density ratio ($\rho_1 = 3$ g/cm^3 and $\rho_2 = 1$ g/cm^3). The computational domain extends $[-8, 20]$ cm with the heavy fluid placed on the left side of the domain and the initial interface at $x = 0$. Unless otherwise stated, the computational grid consists of 100 cells and the adiabatic exponent is $\gamma = 5/3$ for both fluids. The following relation is satisfied in all cases $A_0 g = 1$; thus for the 3:1 density ratio the gravitational acceleration is $g = 2$ cm/s^2.

It is essential to first demonstrate correct behavior of the models for this simple 1D case before more complex problems such as the tilted-rig experiment are considered. Calibration of the models has been performed to match experiments corresponding to $\alpha \sim 0.06$. Additionally, the models are validated against iLES data across a range of mixing parameters. Following Kokkinakis *et al.* [42], calibration of the models is achieved by adjusting the models coefficients to match iLES data. The calibration also takes into account numerical dissipation effects. Subject to careful calibration against iLES data, all models are expected to provide very similar results for the simple 1D RT case.

Comparisons between the models are presented for the volume fraction (VF) and turbulence kinetic energy (K) profiles vs. X/W, as well as for the evolution of the mixing width (W) and maximum turbulence kinetic energy ($K_{\max}$) vs. self-similar time ($A_0 g t^2$). The integral mixing width is defined by $W = \int \tilde{f}_1 \tilde{f}_2 dx$, where $\tilde{f}_1$ is the dense fluid volume fraction and for a binary mixture $\tilde{f}_2 = 1 - \tilde{f}_1$. For self-similar turbulent mixing at a given density ratio, both W and $K_{\max}$ grow at a constant rate equivalent to $A_0 g t^2$.

The flow properties are identical to those previously used in Ref. [42]. The two fluids are considered to be in isentropic hydrostatic equilibrium, i.e., $\tilde{u} = 0$ and $\bar{p}/\bar{\rho}^{\gamma} = \text{const}$ within each fluid, where γ is the ratio of the specific heats ($\gamma = c_p/c_v$).

For the single-fluid turbulence mixing models, within the mixing zone, simple approximations are used to initialize the turbulence variables:

$$K_0 = |A_0| g_x \eta_0, \quad L_0 = \eta_0$$
$$a_{x0} = \sqrt{K_0}/4, \quad b_0 = 10^{-8} \tag{32}$$

where A_0 is the initial Atwood number and η_0 is the perturbation standard deviation of the initial mixing layer $\sigma \approx \varepsilon \lambda_{\max}$, where for $\alpha = 0.06$ in Ref. [16], $\varepsilon = 0.005$ and $\lambda_{\max}$ is half the width of the domain (direction parallel to initial material interface). For a box width of 15 cm, $\eta_0 = 0.00375$ cm.

A. iLES results

A complete description of the iLES can be found in [16]. The iLES results have been obtained using a Lagrange-remap hydrocode [60] called TURMOIL, which calculates the mixing of compressible fluids. The hydrocode solves the Euler equations in conjunction with advection equations for fluid mass fractions.

As in previous iLES studies of RT mixing, the present iLES [16] were conducted by assuming that the Reynolds number is high enough to have little effect on the main quantities and that the flow is beyond the mixing transition as defined by Dimotakis [61] in order for the effect of the Schmidt number to become important. For RT mixing, a suitable definition of the Reynolds number is $\mathrm{Re} = h_1 \dot{h}_1/\nu$, where h_1 is the extent of the mixing zone and ν is the kinematic viscosity. According the experimental results (see Refs. [61,62] and references therein) the mixing transition corresponds to $\mathrm{Re} \sim 10^4$. The results shown in this paper are applicable to high-Reynolds-number mixing in which Re exceeds 10^4.

The iLES results of Ref. [16] are obtained from very high resolution simulations, typically using $2000 \times 1000 \times 1000$ size grids, and it is argued that the results used are grid converged to the point that the effect of the unresolved scales is negligible. For some of the cases considered in Ref. [16], DNS results are also available [18,63] and are very close to iLES.

If mixing is self-similar, then dimensional reasoning suggests that the length scale should be proportional to gt^2. In the RT test case, the depth at time t to which the turbulent mixing zone extends into the denser fluid 1 is given by:

$$h_1 = \alpha A_t g t^2, \tag{33}$$

where ρ_1 and ρ_2 are the densities of the two fluids, g is the acceleration, α is a constant for self-similar mixing, and $A_t = (\rho_1 - \rho_2)/(\rho_1 + \rho_2)$ is the Atwood number.

Experiments using incompressible fluids with low viscosity, low surface tension, and random initial perturbations

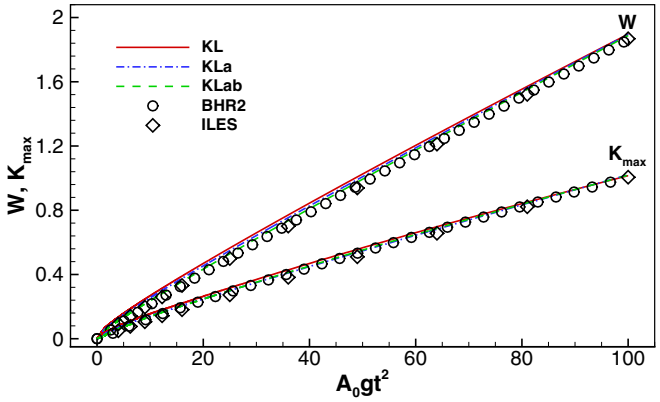

FIG. 1. Self-similar growth of W (cm) and $K_{\max}(\mathrm{cm}^2/\mathrm{s}^2)$.

reveal that the dominant length scale increases as mixing evolves. For RT experiments $\alpha \sim 0.04$ to 0.08; however, when LES or DNS are performed using ideal initial conditions based on small random short-wavelength perturbations, much lower values of $\alpha \sim 0.026$ are obtained [6,16]; this is attributed to the influence of initial conditions. The iLES results [16] used for the models calibration and validation have initial long-wavelength random perturbations at the interface (multimode planar RT mixing) that gives $\alpha \sim 0.06$.

B. Turbulence mixing models results

The self-similar growth rate parameters of the integral mixing width (W) and maximum turbulence kinetic energy ($K_{\max}$) are important physical quantities describing the mixing layer evolution, and it is paramount they are accurately predicted during model calibration. The theory in the self-similar regime of the RT instability indicates that the bubble distance h_b is given by $h_b = aA_tgt^2$; h_b is defined as the most extreme location, where the light fluid penetrates the heavy fluid and is of at least 1% volume fraction. The self-similar RT mixing is typically used for models calibration [42]. Model constants are chosen here to give $a = 0.06$ and the overall degree of molecular mixing and fraction of turbulence dissipated is provided by iLES [16]. W and $K_{\max}$ distributions are presented against aA_tgt^2 rather than t because their self-similar behavior results in a straight line under such scaling.

According to DNS [64], the divergence of velocity is not zero. It is then argued that in RT flows, the mean velocity is purely dilatational and arises solely due to molecular mixing. At very early times, when the density gradients are steep, the mean velocity is important. However, after the early flow development, the Reynolds mean velocity is small so that $\tilde{u}_x \approx a_x$. Therefore, the models are calibrated to give $\tilde{u}_x \approx a_x$. The models coefficient calibration for fluids mixing at an Atwood number of 0.5 (density ratio 3:1) is given in the appendices in Tables III and IV. All models predict the correct self-similar growth (Fig. 1).

Figures 2(a) and 2(b) show the $\tilde{f}$ and K profiles, respectively, at two time instants for the RT case with density ratio 3:1 and initial interface pressure $p_{0i} = 250\ \mathrm{dyn/cm}^2$. The iLES results ($t = 10$s) have been spatially averaged to allow comparisons with the 1D turbulence model calculations.

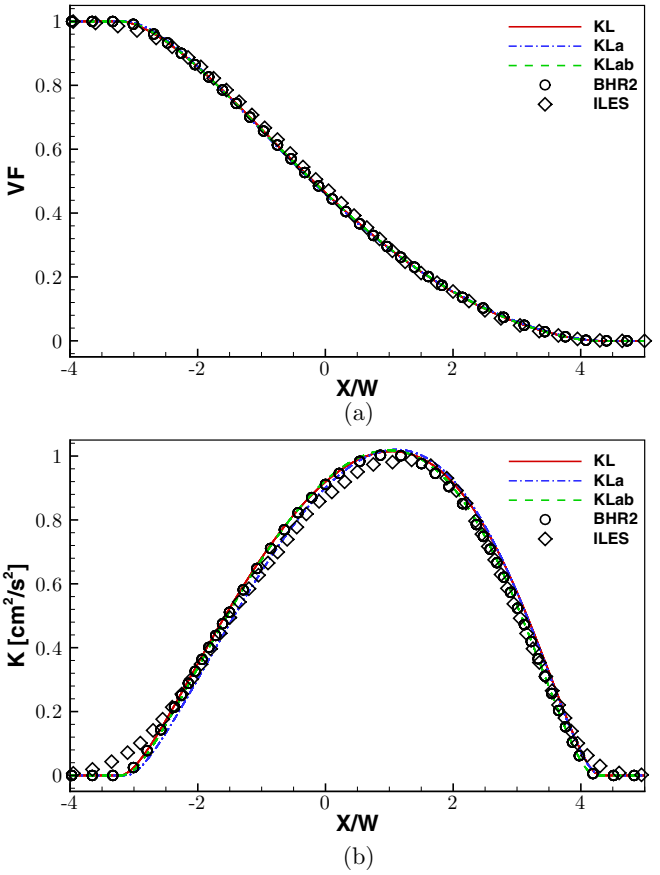

FIG. 2. Profiles of (a) $\tilde{f}$ and (b) K vs. X/W at $t = 10$ s.

The $\tilde{f}$ profile obtained from the different models is almost identical and in excellent agreement with iLES and requires no further investigation.

With respect to K, all models predict similarly the maximum value and its location, as well as the shape of the profile. The maximum K value ($K_{\max}$) is predicted within 4% of the reference averaged iLES solution in all cases. Few minor discrepancies are noticeable. The BHR-2 model underpredicts the magnitude of K on the light-fluid dominated side ($X/W > 0$) near the vicinity of the peak value ($K_{\max}$), while the rest of the models overpredict it on the heavy-fluid dominated side. Overall, the best agreement with iLES is obtained using the BHR-2 model.

The three- and four-equation models are calibrated to give $a_j \approx \tilde{u}_j$ for RTI mixing according to Livescu *et al.* [64]. Note that for 1D incompressible RT flow, $\bar{u}$ should be zero, and hence a equals $\tilde{u}$. The results for the turbulent mass-flux velocity (a_x) and density-specific volume covariance (b) at $t = 10$ s, Figs. 3(a) and 3(b), respectively, show that all models give very similar results.

All models accurately predict both the maximum value and spatial profile of a_x, as well as satisfy $a_x \approx \tilde{u}$ for incompressible RT mixing. For the K-L model, the mass-averaged velocity ($\tilde{u}$) agrees reasonably well with the predictions obtained by the rest of the models and the iLES, with the peak $\tilde{u}$ value being within 5%. For clarity only the BHR-2 model result of $\tilde{u}$ is additionally shown in Fig. 3(a).

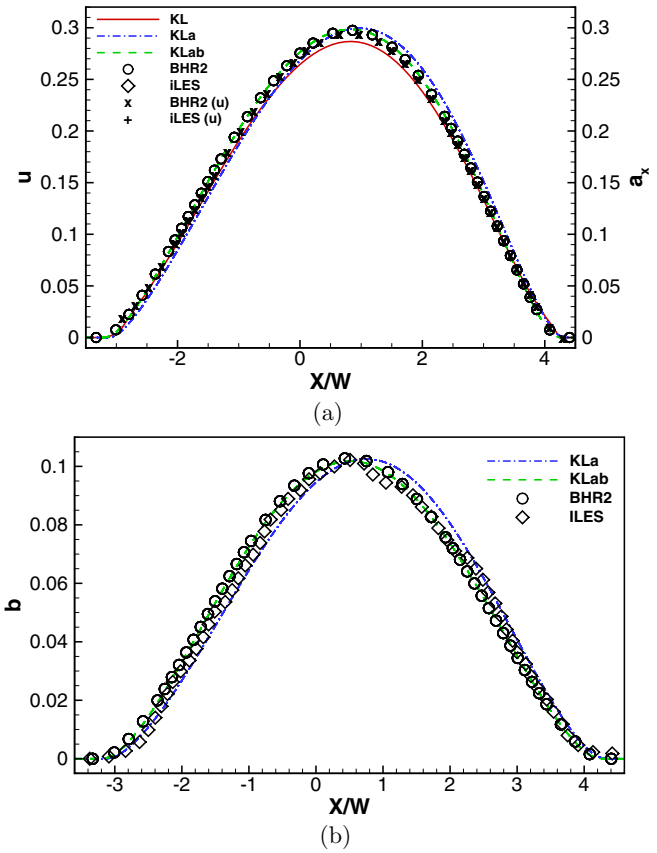

FIG. 3. Profiles of (a) a_x and (b) b vs. X/W at $t = 10$ s.

Note that for the *K-L-a* model the added-mass correction factor in Eq. (20) was set to $c \approx 2.04$, based on the 1D averaged iLES data where $b_{\max}$ occurs.

The models estimated distribution of b at $t = 10$ s [Fig. 3(b)] is also very accurate. The location of $b_{\max}$ is slightly shifted towards the light-fluid dominated side of the mixing layer for the three-equation *K-L-a* model, whereas both of the four-equation models give a much better agreement with the iLES result.

Figure 4 shows that the maximum value of b attains an approximately constant value corresponding to the self-similar state. In the transport equation of b, the three- and

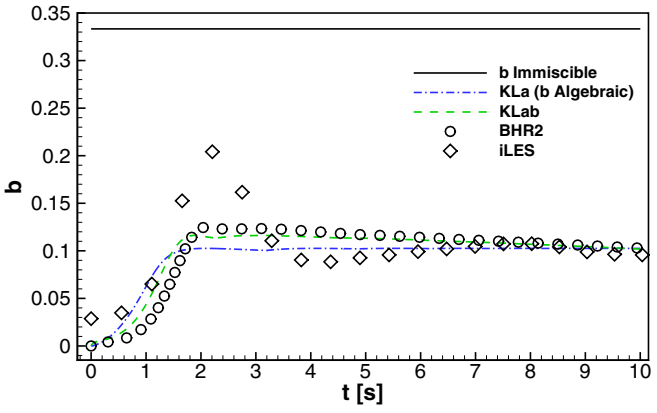

FIG. 4. Time evolution of $b_{\max}$ for self-similar RT mixing.

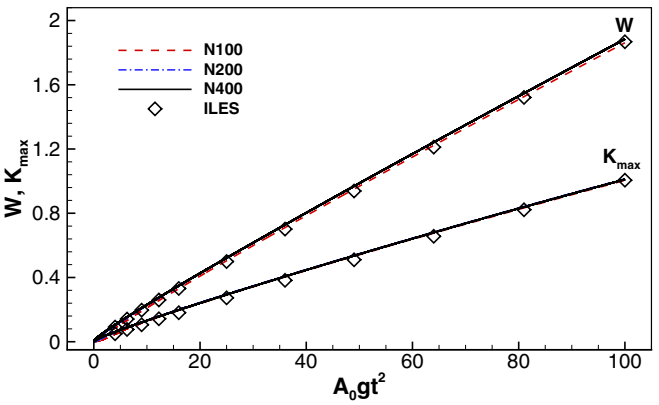

FIG. 5. Time evolution of W (cm) and $K_{\max}(\mathrm{cm}^2/\mathrm{s}^2)$ for RT mixing using the BHR-2 model; effect of grid resolution.

four-equation mixing models include a source (production) term corresponding to the entertainment of unmixed fluids into the mixing layer and, for miscible fluids, a dissipation term corresponding to the destruction caused by molecular mixing. For self-similar mixing, there is a balance between these two processes in so that the value of b at the center of the mixing layer approaches an approximately constant value. The added-mass correction factor "c" in Eq. (20) allows for the adjustment of the maximum attainable value of $b_{\max}$ to account for miscibility.

According to Eq. (21), the maximum (immiscible) value for $b_{\max}$ is $1/3$. However, this value is filtered out during the 1D spatial averaging of the 3D iLES data, thus the maximum value attained after the 1D averaging is $b_{\max} \approx 0.205$ ($t \approx 2$ s).

A grid convergence study was performed for the BHR-2 model using three grids composing of $N_x = 100, 200$, and 400 cells. The reduction in the numerical dissipation associated with the grid size is apparent only at the early stages of the simulation until the turbulent viscosity of the model becomes large enough to surpass that caused by the numerical dissipation of the convection terms. This is evident both in the integral mixing length (W) and the maximum turbulence kinetic energy ($K_{\max}$) in Fig. 5. For $N_x = 100$, the self-similar growth of the BHR-2 is hindered due to the excessive numerical diffusion associated with the coarseness of the grid. Nonetheless, the model shows a clear grid convergence behavior from $N_x =$ 200 to 400 cells. Thus, grid resolution affects the BHR-2 growth rate only at the early stages of the simulation. Once the turbulence viscosity becomes sufficiently large, the targeted self-similar growth rate is achieved.

Calculations using the BHR-2 model were also performed for different initial pressures at the interface in order to assess the incompressibility limit of the model, as well as various heat capacity ratios, and no effect on the results worth commenting was found (plots not shown here).

All models provide similar results for the simple 1D RT problem. The differences with respect to iLES for the mixing width and the maximum turbulent kinetic energy are less than 5%. Small differences between the models and iLES are shown only in the spatial profiles near the edges of the mixing layer.

TABLE I. Tilted-rig case properties.

Acceleration (g_z)	0.034335 cm/ms^2
Heavy fluid density ($\bar{\rho}_H$)	1.89 g/cm^3
Heavy molecular mass (M_H)	246.77673 g/mol
Light fluid density ($\bar{\rho}_L$)	0.66 g/cm^3
Light molecular mass (M_L)	86.176 g/mol
Adiabatic index ($\gamma_H = \gamma_L$)	5/3

TABLE II. Tilted-rig domain size (cm) and grid size.

Grid	L_x	L_z	L_y	N_x	N_z	N_y
RANS	15	24	—	200	320	—
iLES	15	24	15	600	960	600

IV. TILTED-RIG RAYLEIGH-TAYLOR MIXING

The tilted-rig test case originates from a series of experiments [27,40] performed at the Atomic Weapons Establishment in the United Kingdom in the late 1980s to study the mixing between two variable density fluids induced by the Rayleigh-Taylor instability. In the experiment, a tank containing two fluids of different densities, a heavy fluid placed in a tank below a lighter fluid (a stable configuration), is accelerated downwards between two parallel guide rods by firing rocket motors. The downward acceleration caused to the tank, effectively changes the direction of "*gravity*" (external body force) so that the system becomes RT unstable, causing the two fluids to mix. The acceleration from the rocket motors was not constant but averaged approximately 35 times normal gravity. It eventually attains a roughly constant value, but the time during which the acceleration varied is significant and still needs to be considered. One approach is to directly incorporate the measured values into the simulation [i.e., a variable gravity $g(t)$]. This works well for incompressible Navier-Stokes solvers; however, it can create problems for compressible codes. An alternative approach [65] is to make use of a constant acceleration for which a nondimensional time, τ, is used for comparison with experimental results:

$$\tau = \int \sqrt{\frac{A_t g_z}{L_x}} dt + \delta.$$

For the constant gravity case $\delta = 0$. Andrews *et al.* [65] demonstrated that iLES with constant g gives a correct representation of the experiment subject to the above scaling. Following Refs. [16,65], all simulations conducted here use a constant g, thus providing consistent comparisons. Furthermore, the above time scaling enables the comparisons with experiments or incompressible simulations available in the literature. The reader is referred to the experimental images in Refs. [16,65] to make qualitative comparisons with the present results.

The material interface is inclined (tilted) by a few degrees (5.76667°) off the vertical axis to force a large scale two-dimensional overturning motion. Several computational studies using DNS, iLES, and RANS have been carried out for the tilted-rig experiment, e.g., Refs. [18,49,50,65–67]. The iLES results used here are very similar to those given in Refs. [16,65], see Figs. 6–8 in the next section, for example. References [16,65] also provide a detailed comparison of the 3D simulations with the experimental images.

Test case 110 from Refs. [40,65] has been considered in this study. The parameters for computing this case are summarized in Tables I and II. The density of the heavy and light fluids is $\rho_H = 1.89$ g/cm^3 and $\rho_L = 0.66$ g/cm^3, respectively. The Atwood number is $A_t = (\rho_H - \rho_L)/(\rho_H + \rho_L) \approx 0.48$. A near incompressible flow is obtained by using a perfect gas equation of state for each fluid ($\gamma = 5/3$) and a sufficiently high initial interface pressure (20 bar). The volume fractions are calculated by Eq. (7) assuming $M_H/M_L = \rho_H/\rho_L$. The pressure Poisson equation is solved in order to obtain the initial pressure distribution [65]. The turbulence mixing models and iLES simulations described below use a constant vertical acceleration of $g_z = 0.034335$ cm/ms^2, as suggested in Ref. [65] for compressible solvers.

The iLES initial condition is used to obtain the appropriate averaged mean flow quantities. The models are initialized similarly to the 1D RT simulations according to Eq. (32); however here $A_0 \approx 0.517$ and $g = g_z = 0.034335$ cm/ms^2. Additionally, since the initial material interface is "diffuse" (grid resolved), the density-specific volume covariance in the mixed cells is calculated using the two-fluid formulation, Eq. (21), which is consistent with unmixed fluids at t_0. The calibrated values of the models constants from the 1D RT case are used, since the Atwood number between the two cases is similar.

A. iLES results

Youngs [18] demonstrated that subject to sufficient grid resolution for capturing fine-scale structures within the mixing zone, both iLES and DNS give very similar results for quantities such as the mean volume fractions, molecular mixing parameter, and turbulence kinetic energy. Hence, iLES was employed in this study to compute the high-Reynolds behavior of integral properties.

In order to further minimize the numerical uncertainty, we have performed iLES using two different discretization methods in the framework of two different computational codes: TURMOIL, presented in Sec. III A, and CNS3D [11,68]. The latter employs the same numerical methods as those implemented for the turbulence mixing models to solve the Euler equations.

Simulations were performed on a 600×600×960 grid and the results were averaged in the (periodic) y direction. In the x and z directions, a reflective (inviscid wall) boundary condition was imposed. The Mach number is $M = 0.25$, while the Reynolds number is assumed to be Re $\to \infty$, and hence Schmidt number effects are neglected [61].

Let $\bar{\phi}$ be the average of ϕ in the y direction such that $\bar{\phi} = \phi - \phi'$; the Favre average ϕ is given by $\tilde{\phi} = \phi - \phi''$, where $\tilde{\phi} = \overline{\rho\phi}/\bar{\rho}$; the molecular mixing parameter (θ) is calculated by:

$$\theta = (\overline{f_1 f_2})/(\bar{f}_1 \bar{f}_2). \tag{34}$$

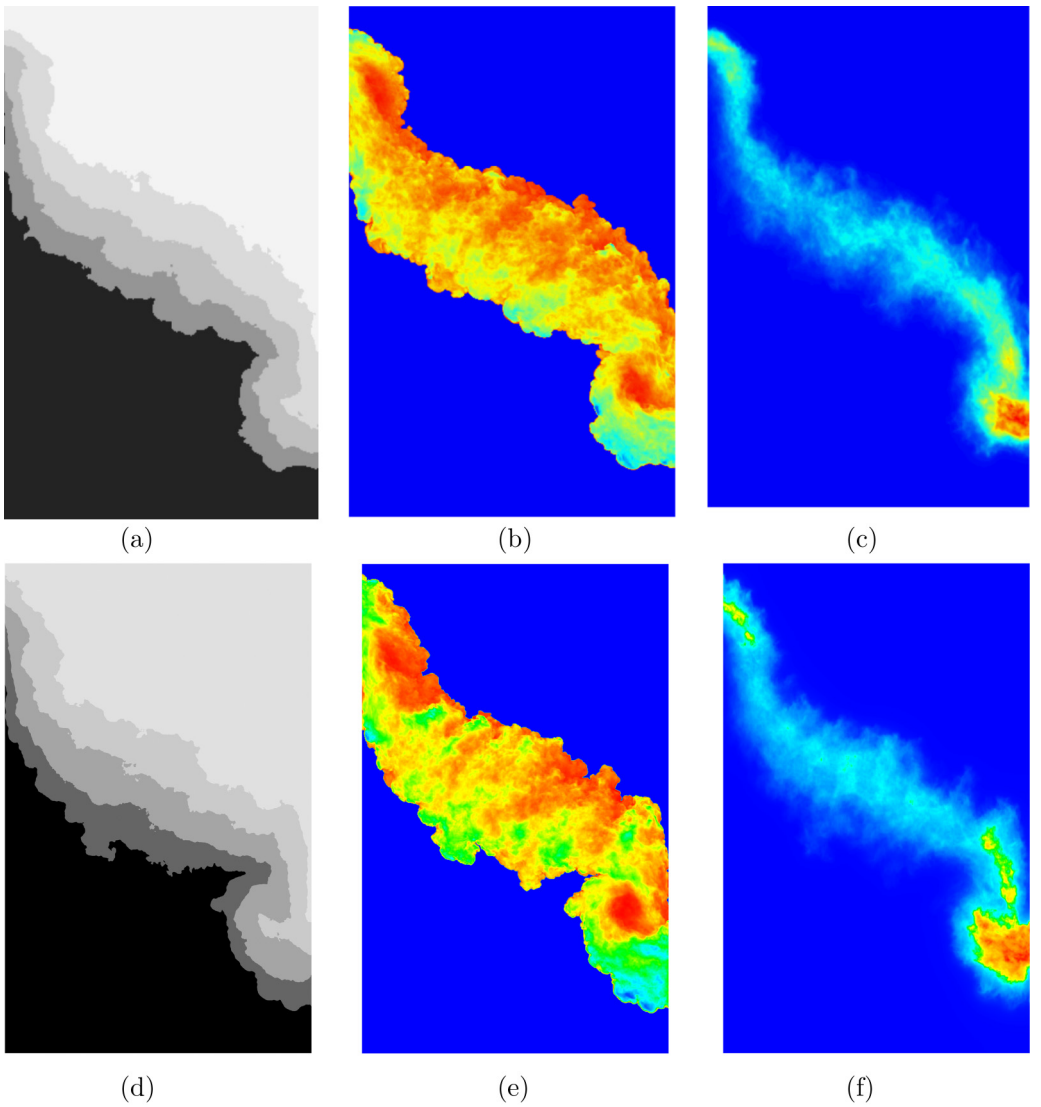

FIG. 6. Contour plots of $\bar{f}$, θ, and $\tilde{k}$ at $\tau = 1.741$ using [(a)–(c)] TURMOIL [65] and [(d)–(f)] CNS3D, respectively.

The turbulence kinetic energy ($\tilde{k}$) and density specific-volume covariance (b) are calculated by:

$$\tilde{k} = \frac{1}{2}\overline{\rho[(u_x - \tilde{u}_x)^2 + u_y^2 + (u_z - \tilde{u}_z)^2]}/\bar{\rho} \tag{35}$$

and

$$b = -\overline{\rho'(1/\rho)'}. \tag{36}$$

Let $\bar{\bar{\phi}}(z)$ denote the ensemble average of ϕ over the x-y plane; then the left (spike) and right (bubble) plume penetrations (H_s and H_b) measure the location where $\bar{\bar{f}}_1 = 0.001$ and $\bar{\bar{f}}_2 = 0.001$; $f_1 = f_H$ and $f_2 = f_L$ are the volume fractions of the heavy and light fluids, respectively.

The integral mixing width (W) in this case is given by:

$$W = \int \bar{f}_1 \bar{f}_2 \, dxdz/L_x. \tag{37}$$

Both iLES codes give a similar position for the location of the plumes at the beginning ($\tau = 0$–0.4) and at the end of the simulation ($\tau \approx 1.9$) (Fig. 7). Some discrepancies appear only in the time window of 0.4–1.9.

The integral mixing width given by TURMOIL increases faster than CNS3D at $\tau < 0.5$, when the Mach number is $M \ll 0.1$ and the inertial range is not resolved (Fig. 8). For $\tau > 1.5$, however, CNS3D resolves the finer scales better, thus predicting a faster growth of W. The above agrees with the conclusions drawn in Ref. [69] for a double vortex pairing mixing layer. This behavior is also reflected by the larger value of K obtained at $\tau = 1.741$ [cf. Fig. 6(f) and Fig. 6(c)], as well as the thickness of the turbulent mixing layer [Fig. 6(d)].

The two iLES codes provide very similar results for the volume fraction [Figs. 6(a) and 6(d)] and local molecular mixing parameter [Figs. 6(b) and 6(e)]. The largest discrepancy appears around the location where the maximum θ occurs in the bubble plume.

The initial slower growth of the mixing zone observed in the compressible Eulerian code (CNS3D) leads to an accumulation of potential energy. As the local Mach increases, the stored potential energy is "released," thus causing the observed larger growth rate in the integral mix width (W)

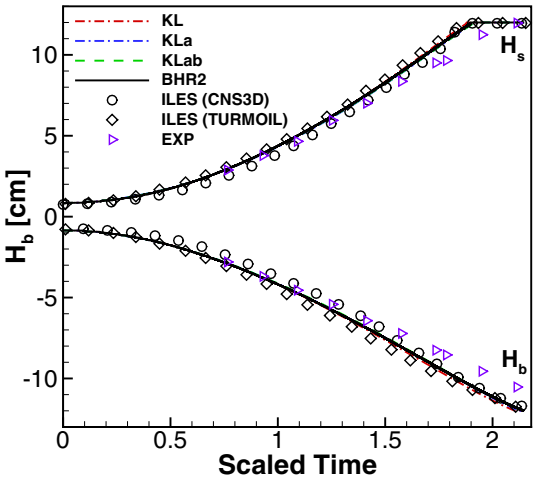

FIG. 7. Bubble and spike plumes position vs. scaled time (τ).

at late time. Overall, the Lagrange-remap code (TURMOIL) predicts more accurately the evolution of the mixing zone with time.

B. Results: Turbulence mixing models

Figure 7 shows the distance of the bubble plume's leading edge (H_b), which forms at the lower right of the mixing layer [see Figs. 6(a) and 6(d) for illustration]. The experimental values plotted are obtained from Ref. [65]. The results from all models are in good agreement with iLES. Excellent accuracy is also achieved by all models in capturing the position of the spike plume (H_s) that forms in the upper-left corner of the mixing layer.

The results for the integral mixing width W (Fig. 8) show only small differences between the models, with the *K-L* and BHR-2 models being in closer agreement with iLES (CNS3D). The difference between CNS3D and TURMOIL is due to their different numerical dissipation properties. The differences between the models and iLES for the mixing width, and the position of bubble and spike plumes are no greater than 4%.

Comparisons of the Favre-averaged mass-fraction ($\tilde{F}$) profiles between the models and iLES at $\tau = 1.741$ are shown

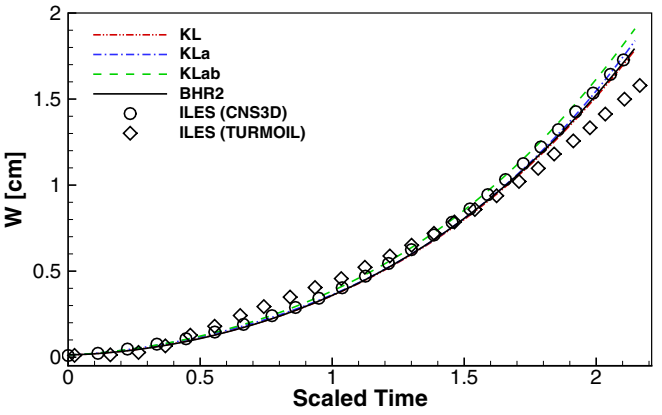

FIG. 8. Integral mixing width (W) vs. scaled time (τ).

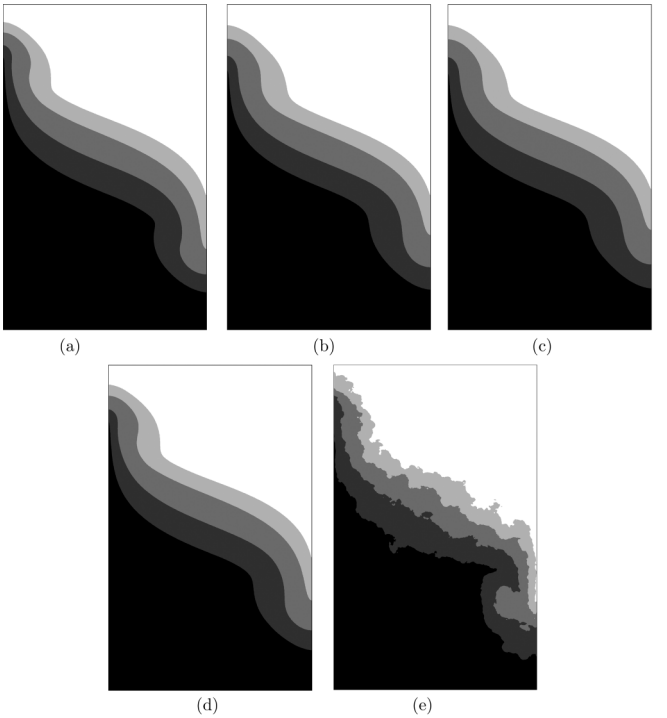

FIG. 9. Mass fraction ($\tilde{F}_H$) contour plot at $\tau = 1.741$; (a) *K-L*, (b) *K-L-a*, (c) *K-L-a-b*, (d) BHR-2, and (e) iLES.

in Fig. 9. The results at earlier times are very similar. All contour plots are normalized by a reference value, and the isocontour levels shown here are 0.025, 0.3, 0.7, and 0.975, unless otherwise stated. The *K-L* and BHR-2 models give

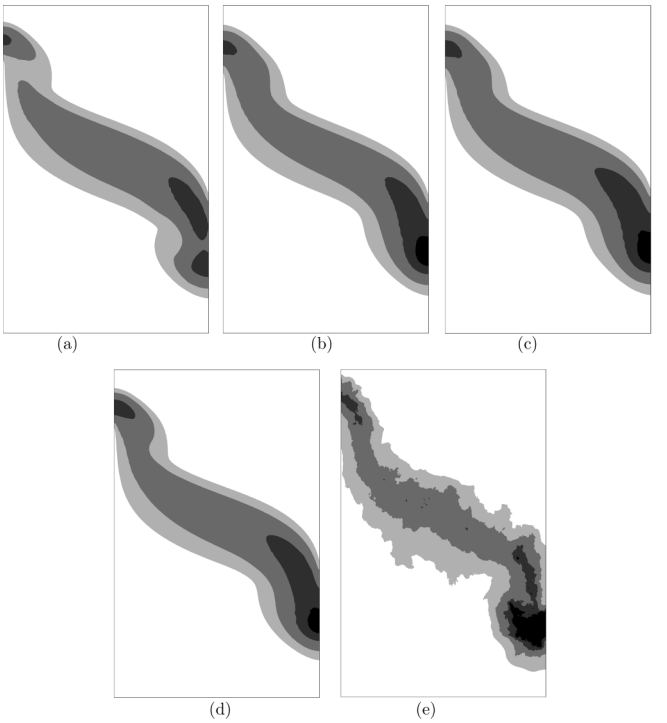

FIG. 10. K/K_{ref} ($K_{\text{ref}} = 2.114\ \text{cm}^2/\text{ms}^2$) at $\tau = 1.741$; (a) *K-L*, (b) *K-L-a*, (c) *K-L-a-b*, (d) BHR-2, and (e) iLES.

the best results for the overturning spike and bubble plumes. None of the models seem capable of accurately predicting the bubble plume region due to the excessive isotropic turbulent diffusion; however, the thickness of the mass-fraction layers across the remainder of the mixing zone is accurately captured, including the spike plume. In the planar tilted region, where the mixing is mostly 1D (homogeneous in two directions), the differences between the models are negligible.

The K profiles are shown in Fig. 10. The K/K_{ref} values predicted by all turbulence models are consistent with iLES throughout the mixing layer. The BHR-2 model predicts a width and a shape of the K/K_{ref} isocontours closer to iLES than the rest of the models. In the region just above the bubble plume (lower-right "*neck*"), iLES exhibits a narrow tail-like feature corresponding to contour level 0.75 (dark gray). Apart from the two-equation *K-L* model, all the other models predict a single merged region. The discrepancy is due to the overprediction of K, hence turbulent diffusion, at the "neck" by the three- and four-equation models, which causes the two distinct $K/K_{\text{ref}} = 0.75$ contour level regions to merge. Since the "neck" region is highly two-dimensional, it exemplifies whatever effect the cross-terms have on the models results, which otherwise vanishes in the 1D simulations. In contrast, in the region just below the spike plume (upper-left "neck"), all models agree reasonably well with the iLES solution apart from the *K-L*; the BHR-2 model provides the most accurate representation of iLES. Further analysis needs to be carried out in order to draw an accurate understanding of the models behavior at the highly 2D "neck" regions.

The maximum vertical turbulent mass-flux velocity, $\max(a_z)$, is accurately predicted by all models (Fig. 11), with the BHR-2 model showing the closest agreement with the iLES results at the large-scale bubble and spike plumes. There is some uncertainty regarding the iLES statistics at late time due to the integral length scale becoming large compare to the spanwise domain size. This explains the patches of large a_z/a_z^{ref} that can be observed in the iLES contour plot [Fig. 11(d)]. Whether a larger domain size ($L_y \gg 15$ cm) can result in additional large-a_z contour patches in the tilted mixing region of the 2D-averaged iLES and form a single merged contour level as the BHR-2 model predicts remains to be investigated.

With regards to the b parameter, each model is found to behave slightly differently but still provide a reasonable estimate (Fig. 12). The algebraic formulation used in the *K-L-a* model for b is evident by the uniform distribution along the mixing layer. The added-mass correction factor value used by the *K-L-a* model is set to $c \approx 2.04$ here, too, despite the different fluid partial densities compared to the 1D-RT case. Note that Eq. (20) can be written in terms of the mass and volume fractions only, and therefore it is independent of

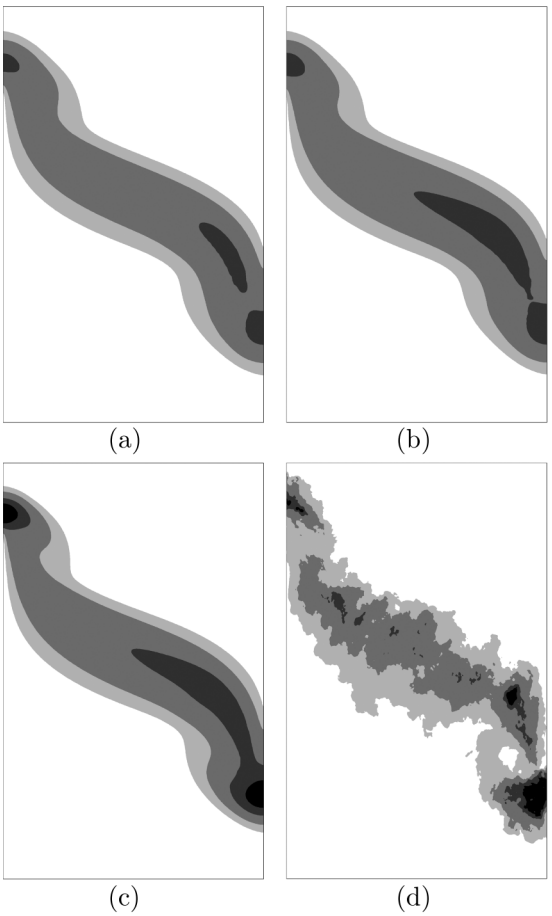

FIG. 11. $a_z/a_z^{\text{ref}}(a_z^{\text{ref}} = 0.5$ m/s) at $\tau = 1.741$; (a) *K-L-a*, (b) *K-L-a-b*, (c) BHR-2, and (d) iLES.

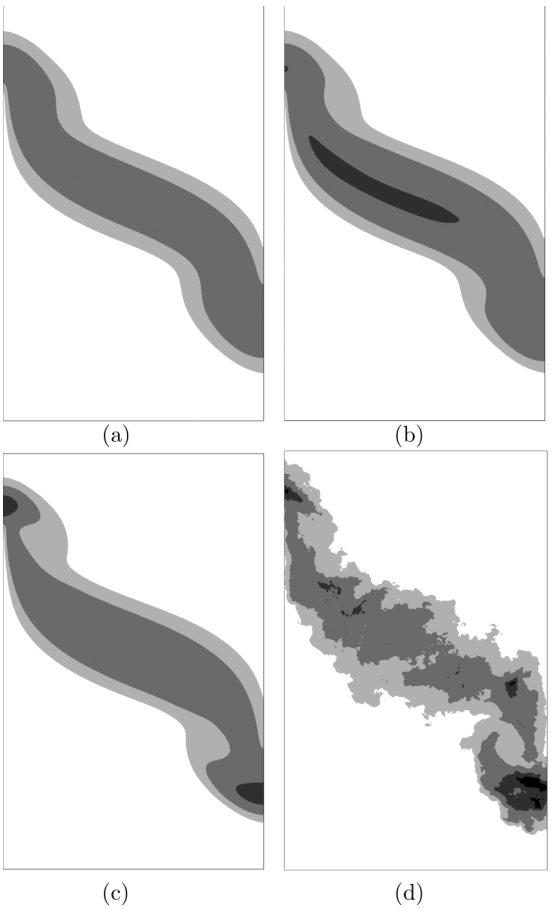

FIG. 12. b/b_{ref} ($b_{\text{ref}} = 0.16$) at $\tau = 1.741$; (a) *K-L-a*, (b) *K-L-a-b*, (c) BHR-2, and (d) iLES.

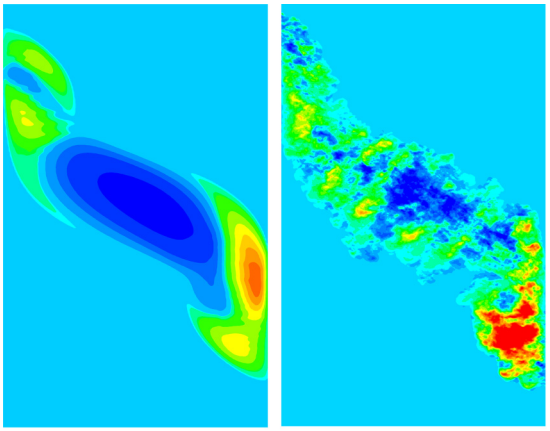

(a) (b)

FIG. 13. a_x contours at $\tau = 1.741$; minimum (blue) -0.05 m/s, maximum (red) 0.15 m/s; (a) BHR-2, and (b) iLES.

density. For Atwood numbers other than $A \simeq 0.5$ as examined here, the value of c would require adjustment. The *K-L-a-b* model predicts a narrow band of large b in the tilted region that can be argued to correspond to the few patches of larger b observed in the iLES. BHR-2 is the only model that correctly predicts the large values of b at the spike and bubble plumes according to the reference iLES solution.

The BHR-2 model predicts with reasonable accuracy a_x, including the area of negative countergradient mass-flux velocity at the top of the tilted mixing layer (Fig. 13). However, the model is not able to predict the positive flux in the lower half of the tilted mixing region, where, as suggested by Denissen *et al.* [50], it may account for some of the differences in the mass-fraction contours. Furthermore, the location of the maximum a_x value, as well as the positive value at the front of the spike plume do not agree with the reference iLES solution either.

The effects of the MSTD proposed by Bertsch and Gore [39] are briefly discussed below. MSTD replaces the standard Fickian-like mass-fraction turbulent transport term by Eq. (27) and can be implemented in conjunction with any turbulence model that includes a transport equation for the turbulent mass-flux velocities (a_i). Here the GDA and MSTD assumptions are compared in the framework of the BHR-2 model, which has given overall the most promising results this far.

Figure 14 shows that the MSTD term significantly improves the distribution of $\tilde{F}$ in the bubble and spike plumes at the expense of a slight increase of the mixing zone width. The MSTD modification has hardly any effect on the turbulence kinetic energy profiles (plots not shown here). The S_F limiter also offers some improvement to the BHR-2 model, particularly the large 2D overturning bubble and spike plume features; however, the best results for the mass fraction in the plume regions (with reference to iLES) are obtained by the BHR-2 model with the MSTD approximation.

V. CONCLUSIONS

This study examined the accuracy of two- to four-equation (linear eddy viscosity) turbulence models for Rayleigh-Taylor–induced turbulent mixing through comparisons with high-resolution simulations.

By increasing model complexity in a gradual and systematic manner, a detailed understanding of the accuracy and limitations of the models is obtained. Discretization of the governing and turbulence model equations is kept consistent across all models, thus reducing accuracy uncertainties associated with the numerical implementation.

The main conclusions drawn from the investigation are summarized below:

(i) The more complex tilted-rig test case was necessary in order to reveal discrepancies between the models.

(ii) The *K-L-a* model [45] provides better accuracy than the *K-L* model and also employs a simpler form of the turbulence kinetic energy production source term. This is evident by comparing with the production source term, S_K, used in Refs. [32,42].

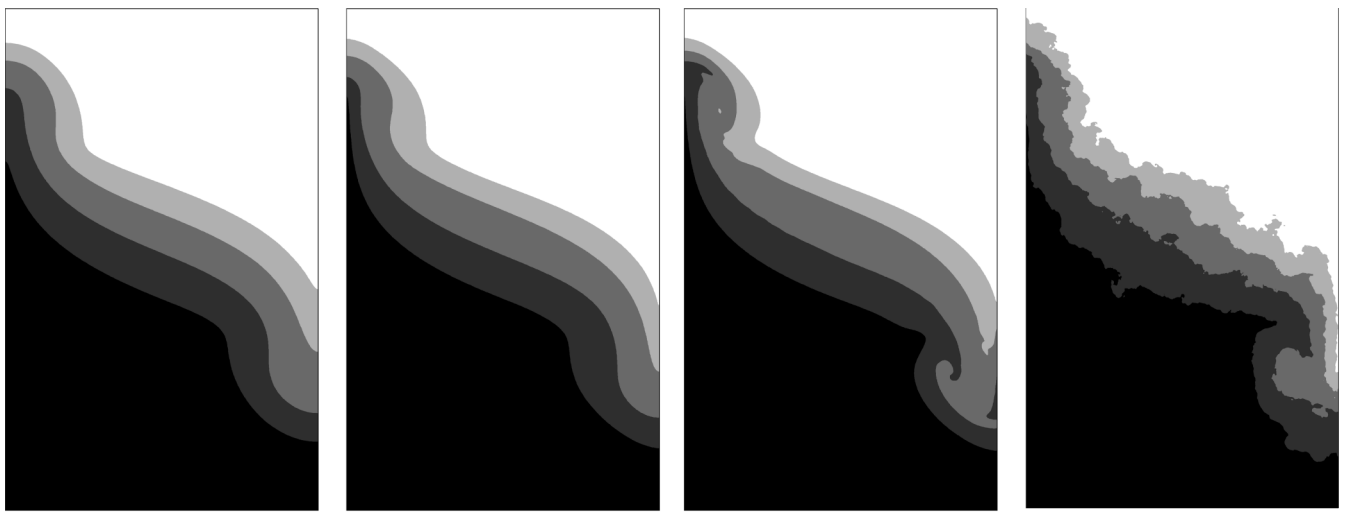

(a) (b) (c) (d)

FIG. 14. Mass fraction ($\tilde{F}_H$) at $\tau = 1.741$; (a) BHR-2, (b) BHR-2 with S_F, (c) BHR-2 with MSTD, and (d) iLES.

TABLE III. Diffusion coefficients (all models).

Diffusion L (N_L)	0.125
Diffusion K (N_K)	1.1
Diffusion $\tilde{h}$, F, a, b (N_ϕ)	1.0

(iii) The *K-L-a-b* model presented here is a reduced form of the BHR-2 model. Using a model transport equation for b provides some accuracy improvement compare to the algebraic expression used by the *K-L-a* model, particularly in relation to the prediction of the turbulent mass-flux velocities and the turbulence kinetic energy results in the tilted-rig test case.

(iv) With respect to the tilted-rig case, the BHR-2 model performs better than *K-L-a-b* in the spike but worse in the bubble plume region.

(v) The turbulent viscosity limiter (S_F) improves the mass-fraction predictions, particularly in the plume regions of the tilted-rig case.

(vi) The modified species turbulent diffusion term improved the mass-fraction results, particularly in the large-scale 2D overturning regions of the mixing layer, without adversely affecting the accuracy of the rest of the results.

(vii) Overall, the BHR-2 model provided the closest results to iLES in the bubble and spike plume regions.

Future work is required to address accuracy issues regarding the prediction of (positive) a_x in the lower half of the tilted mixing region and to further examine the modified species turbulent diffusion term, as well as the effect of the models cross-terms in highly 2D regions.

TABLE IV. Models coefficients for density ratio 3:1.

	K-L	*K-L-a*	*K-L-a-b*	BHR-2
Eddy viscosity (C_μ)	0.55	0.61	0.60	0.60
Drag (C_D)	1.24	0.65	0.66	0.66
Buoyancy (C_B)	1.0	1.58	1.58	1.58
Production L 1 (C_L)	1.0	1.0	1.0	0.28
Production L 2 (C_{L1})	⋯	⋯	⋯	0.06
Production L 3 (C_{L4})	⋯	⋯	⋯	0.48
Destruction a (C_{Da})	⋯	1.35	1.39	1.39
Destruction b (C_{Db})	⋯	⋯	1.37	1.37
Redistribution a (C_{Ra})	⋯	⋯	⋯	−0.05
Redistribution b (C_{Rb})	⋯	⋯	⋯	0.05

ACKNOWLEDGMENTS

Dimitris Drikakis wishes to express his gratitude and appreciation to the Atomic Weapons Establishment for their financial support through the William Penney Fellowship award. The manuscript contains material ©British Crown Owned Copyright 2018/AWE, reproduced with permission. Results were obtained using the EPSRC funded ARCHIE-WeSt High Performance Computer (www.archie-west.ac.uk) under EPSRC Grant No. EP/K000586/1.

APPENDIX: CALIBRATED MODELS CONSTANTS

(⋯) indicates constants not applicable to the model.

[1] P. Amendt, J. D. Colvin, R. E. Tipton, D. E. Hinkel, M. J. Edwards, O. L. Landen, J. D. Ramshaw, L. J. Suter, W. S. Varnum, and R. G. Watt, Phys. Plasmas **9**, 2221 (2002).
[2] V. Smalyuk, O. Hurricane, J. Hansen, G. Langstaff, D. Martinez, H.-S. Park, K. Raman, B. Remington, H. Robey, O. Schilling, R. Wallace, Y. Elbaz, A. Shimony, D. Shvarts, C. D. Stefano, R. Drake, D. Marion, C. Krauland, and C. Kuranz, High Energy Density Phys. **9**, 47 (2013).
[3] J. Decaix and E. Goncalvès, Int. J. Numer. Methods Fluids **68**, 1053 (2012).
[4] J. R. Nanduri, D. R. Parsons, S. L. Yilmaz, I. B. Celik, and P. A. Strakey, Combust. Sci. Technol. **182**, 794 (2010).
[5] A. S. Almgren, J. B. Bell, C. A. Rendleman, and M. Zingale, Astrophys. J. **637**, 922 (2006).
[6] W. H. Cabot and A. W. Cook, Nat. Phys. **2**, 562 (2006).
[7] J. M. Pittard, S. A. E. G. Falle, T. W. Hartquist, and J. E. Dyson, Mon. Not. R. Astron. Soc. **394**, 1351 (2009).
[8] M. Brüggen, E. Scannapieco, and S. Heinz, Mon. Not. R. Astron. Soc. **395**, 2210 (2009).
[9] J. Ferziger, J. Koseff, and S. Monismith, Comput. Fluids **31**, 557 (2002).
[10] F. Grinstein, L. Margolin, and W. Rider, *Implicit Large Eddy Simulation: Computing Turbulent Fluid Dynamics* (Cambridge Univeristy Press, Cambridge, 2007).
[11] D. Drikakis, M. Hahn, A. Mosedale, and B. Thornber, Philos. Trans. R. Soc. Lond. A **367**, 2985 (2009).
[12] B. Thornber, D. Drikakis, D. Youngs, and R. Williams, J. Fluid Mech. **654**, 99 (2010).
[13] M. Lombardini, D. J. Hill, D. I. Pullin, and D. I. Meiron, J. Fluid Mech. **670**, 439 (2011).
[14] M. Lombardini, D. I. Pullin, and D. I. Meiron, J. Fluid Mech. **690**, 203 (2012).
[15] A. Hadjadj, H. C. Yee, and B. Sjögreen, Int. J. Numer. Methods Fluids **70**, 1405 (2012).
[16] D. L. Youngs, Philos. Trans. R. Soc. A **371**, 20120173 (2013).
[17] F. F. Grinstein, A. A. Gowardhan, and J. R. Ristorcelli, Philos. Trans. R. Soc. A **371**, 20120217 (2013).
[18] D. L. Youngs, Phys. Scr. **92**, 074006 (2017).
[19] T. J. Rehagen, J. A. Greenough, and B. J. Olson, J. Fluids Eng. **139**, 061204 (2017).
[20] B. E. Morgan, B. J. Olson, J. E. White, and J. A. McFarland, J. Turbul. **18**, 973 (2017).
[21] Y. Zhou, Phys. Rep. **720–722**, 1 (2017).
[22] Y. Zhou, Phys. Rep. **723–725**, 1 (2017).
[23] U. Alon, J. Hecht, D. Ofer, and D. Shvarts, Phys. Rev. Lett. **74**, 534 (1995).
[24] J. D. Ramshaw, Phys. Rev. E **58**, 5834 (1998).
[25] G. Dimonte and M. Schneider, Phys. Fluids **12**, 304 (2000).

[26] B. Cheng, J. Glimm, and D. H. Sharp, Chaos **12**, 267 (2002).
[27] D. Youngs, Physica D **37**, 270 (1989).
[28] D. Youngs, Laser Part. Beams **12**, 725 (1994).
[29] Y. Chen, J. Glimm, D. H. Sharp, and Q. Zhang, Phys. Fluids **8**, 816 (1996).
[30] A. Llor, *Statistical Hydrodynamic Models for Developing Mixing Instability Flows* (Springer, Berlin, 2005).
[31] S. Gauthier and M. Bonnet, Phys. Fluids A **2**, 1685 (1990).
[32] G. Dimonte and R. Tipton, Phys. Fluids **18**, 085101 (2006).
[33] J. T. Morán-López and O. Schilling, High Energy Density Phys. **9**, 112 (2013).
[34] J. Morán-López and O. Schilling, Shock Waves **24**, 325 (2014).
[35] *Computational Fluid Dynamics*, edited by G. de Vahl Davis and C. Fletcher, Math. Comput. Simul. (North-Holland, Amsterdam, 1989), Vol. 31, p. 140.
[36] A. Banerjee, R. A. Gore, and M. J. Andrews, Phys. Rev. E **82**, 046309 (2010).
[37] J. D. Schwarzkopf, D. Livescu, R. A. Gore, R. M. Rauenzahn, and J. R. Ristorcelli, J. Turbul. **12**, N49 (2011).
[38] K. Stalsberg-Zarling and R. A. Gore, The bhr2 turbulence model Incompressible isotropic decay, Rayleigh-Taylor, Kelvin-Helmholtz and homogeneous variable density turbulence, Report LA-UR-11-04773 (LANL, 2011).
[39] R. L. Bertsch and R. A. Gore, RANS simulations of Rayleigh-Taylor Instability Subject to a changing body force, Report LA-UR-16-24705 (LANL, 2016).
[40] V. Smeeton and D. Youngs, Experimental Investigation of Turbulent Mixing by Rayleigh-Taylor Instability, Part 3, Report O 35/87 (AWE, 1987).
[41] G. Allaire, S. Clerc, and S. Kokh, J. Comput. Phys. **181**, 577 (2002).
[42] I. W. Kokkinakis, D. Drikakis, D. L. Youngs, and R. J. Williams, Int. J. Heat Fluid Flow **56**, 233 (2015).
[43] F. A. Williams, *Combustion Theory*, 2nd ed. (CRC Press, Boca Raton, Florida, 1994).
[44] A. W. Cook, Phys. Fluids **21**, 055109 (2009).
[45] B. E. Morgan and M. E. Wickett, Phys. Rev. E **91**, 043002 (2015).
[46] B. E. Morgan, O. Schilling, and T. A. Hartland, Phys. Rev. E **97**, 013104 (2018).
[47] J. D. Schwarzkopf, D. Livescu, J. R. Baltzer, R. A. Gore, and J. R. Ristorcelli, Flow, Turbul. Combust. **96**, 1 (2016).
[48] D. Besnard, F. H. Harlow, R. M. Rauenzahn, and C. Zemach, Turbulence transport equations for variable-density turbulence and their relationship to two-field models, Report LA-12303-MS (LANL, 1992).
[49] B. Rollin, N. A. Denissen, J. M. Reisner, and M. J. Andrews, in *ASME International Mechanical Engineering Congress and Exposition*, Vol. 7 Fluids and Heat Transfer, Parts A, B, C, and D (ASME, Houston, Texas, 2012), pp. 1353–1361.
[50] N. A. Denissen, B. Rollin, J. M. Reisner, and M. J. Andrews, J. Fluids Eng. **136**, 091301 (2014).
[51] B. Vreman, B. Geurts, and H. Kuerten, J. Fluid Mech. **278**, 351 (1994).
[52] S. Godunov, Mat. Sb **47**, 134 (1959).
[53] K. Kim and C. Kim, J. Comput. Phys. **208**, 570 (2005).
[54] B. Thornber, A. Mosedale, D. Drikakis, D. Youngs, and R. Williams, J. Comput. Phys. **227**, 4873 (2008).
[55] E. Toro, M. Spruce, and W. Speares, Shock Waves **4**, 25 (1994).
[56] D. Drikakis and W. Rider, *High-Resolution Methods for Incompressible and Low Speed Flows* (Springer, Berlin, 2005).
[57] M. Hahn and D. Drikakis, Int. J. Numer. Methods Fluids **47**, 971 (2005).
[58] M. Hahn, D. Drikakis, D. Youngs, and R. Williams, Phys. Fluids **23**, 046101 (2011).
[59] E. Shapiro and D. Drikakis, J. Comput. Phys. **210**, 584 (2005).
[60] D. L. Youngs, Phys. Fluids A **3**, 1312 (1991).
[61] P. Dimotakis, J. Fluid Mech. **409**, 69 (2000).
[62] A. Cook and P. Dimotakis, J. Fluid Mech. **443**, 69 (2001).
[63] D. Livescu, Philos. Trans. R. Soc. A **371**, 20120185 (2013).
[64] D. Livescu, J. R. Ristorcelli, R. A. Gore, S. H. Dean, W. H. Cabot, and A. W. Cook, J. Turbul. **10**, N13 (2009).
[65] M. J. Andrews, D. L. Youngs, D. Livescu, and T. Wei, J. Fluids Eng. **136**, 091212 (2014).
[66] J. M. Holford, S. B. Dalziel, and D. L. Youngs, Laser Part. Beams **21**, 419 (2003).
[67] T. Wei and D. Livescu, APS Meeting Abstracts (2011).
[68] D. Drikakis, Progr. Aerospace Sci. **39**, 405 (2003).
[69] P. Tsoutsanis, I. W. Kokkinakis, L. Könözsy, D. Drikakis, R. J. Williams, and D. L. Youngs, Comput. Methods Appl. Mech. Eng. **293**, 207 (2015).